# High- and low-latitude forcing of the Nile River regime during the Holocene inferred from laminated sediments of the Nile deep-sea fan

Cécile L. Blanchet [a,b,*], Rik Tjallingii [b], Martin Frank [a], Janne Lorenzen [a,1], Anja Reitz [a], Kevin Brown [a], Tomas Feseker [a,2], Warner Brückmann [a]

[a] GEOMAR | Helmholtz Centre for Ocean Research Kiel, Wischhofstraße 1-3, 24148 Kiel, Germany
[b] NIOZ-Royal Netherlands Institute for Sea Research, Landsdiep 4, 1797 SZ 't Hoorntje (Texel), The Netherlands

## ARTICLE INFO

## ABSTRACT

Sediments deposited on deep-sea fans are an excellent geological archive to reconstruct past changes in fluvial discharge. Here we present a reconstruction of changes in the regime of the Nile River during the Holocene obtained using bulk elemental composition, grain-size analyses and radiogenic strontium (Sr) and neodymium (Nd) isotopes from a sediment core collected on the Nile deep-sea fan. This 6-m long core was retrieved at ∼700 m water-depth and is characterized by the presence of a 5-m thick section of finely laminated sediments, which were deposited between 9.5 and 7.3 ka BP and correspond to the African Humid Period (AHP). The data show distinct changes in eolian dust inputs as well as variations in discharge of the Blue Nile and White Nile. Sedimentation was mainly controlled by changes in fluvial discharge during the Holocene, which was predominantly forced by low-latitude summer insolation and by the location of the eastern African Rain Belt. The changes in relative contribution from the Blue Nile and White Nile followed changes in low-latitude spring/autumn insolation, which highlights the role of changes in seasonality of the precipitation on the Nile River regime. The relative intensity of the Blue Nile discharge was enhanced during the early and late Holocene at times of higher spring insolation (with massive erosion and runoff during the AHP at times of high summer insolation), while it was reduced between 8 and 4 ka at times of high autumn insolation. The gradual insolation-paced changes in fluvial regime were interrupted by a short-term arid event at 8.5–7.3 ka BP (also associated with rejuvenation of bottom-water ventilation above the Nile fan), which was likely related to northern hemisphere cooling events. Another arid event at 4.5–3.7 ka BP occurred as the apex of a gradually drier phase in NE Africa and marks the end of the AHP.

© 2013 Elsevier B.V. All rights reserved.

## 1. Introduction

Due to the fact that atmospheric temperatures remained near constant during the Holocene (last 10 kyr), this interval is generally considered as climatically stable as compared to the rest of the Quaternary (Grootes et al., 1993). However, environmental and hydrological reconstructions have revealed that subtropical regions have drastically changed during the course of the Holocene (Haug et al., 2001; Ruddiman, 2003). In particular, the progressive drying of North Africa led to the retreat of the vegetation cover and of human populations from the so-called 'Green Sahara' (Gasse, 2000; Kuper and Kröpelin, 2006). Paleoenvironmental and archeological studies documented the occurrence of a very wet phase in North Africa between 10 and 6 ka BP, which led to the development of extensive lake and river systems and of a savannah-type of vegetation within what is nowadays one of the most arid areas on Earth (Drake et al., 2011). This pronounced Holocene wet phase is known as the African Humid Period (AHP) and favored the settlement of Neolithic human populations within the present-day Saharan Desert (Kuper and Kröpelin, 2006). Additionally, the highly increased Nile River runoff had a major impact on the marine environment in the Eastern Mediterranean, as evidenced by the deposition of organic-rich sapropel layers (Rossignol-Strick et al., 1982). Stratification of the water column and high primary productivity in the surface waters induced oxygen depletion of the bottom waters in the Eastern Mediterranean basin, which stimulated the accumulation and preservation of organic matter in the sediments (De Lange et al., 2008).

* Corresponding author at: NIOZ-Royal Netherlands Institute for Sea Research, Landsdiep 4, 1797 SZ 't Hoorntje (Texel), The Netherlands. Tel.: +31 222 369583.
E-mail addresses: cblanchet@geomar.de, cblanchet@nioz.nl (C.L. Blanchet).
[1] Now at: Christian-Albrechts-University of Kiel, Institute of Geosciences, Department of Marine Micropaleontology, Ludewig-Meyn-Straße 14, 24118 Kiel, Germany.
[2] Now at: University of Bremen, Department of Geosciences, Klagenfurter Straße, 28359 Bremen, Germany.

The termination of the AHP was marked by a southward shift of the African monsoon and associated rainfall belts causing a retreat of the extensive Saharan grassland and the desiccation of vast system of lakes and rivers within the Sahara (Pachur and Kröpelin, 1987; Lézine et al., 2011). The primary forcing for this wet/arid transition is thought to be the precession-forced low latitude insolation, which gradually decreased between 8 and 4 ka BP (Rossignol-Strick, 1983). However, the rate of the paleoenvironmental changes appears to be highly variable depending on the archives and on the studied area (Lézine et al., 2011). Consequently, the response of continental environments and ecosystems to a gradual orbital forcing is still under debate. Some authors reported a gradual transition, which implies a linear response of the ecosystem to the orbital forcing (Brovkin et al., 2002; Fleitmann et al., 2003; Renssen et al., 2003; Kröpelin et al., 2008), whereas others reported a more abrupt transition, which suggests the existence of complicated feedback processes and threshold responses between the ecosystem and the climate (Gasse and Van Campo, 1994; Claussen et al., 1999; deMenocal et al., 2000a; Liu et al., 2007).

Here we focus on changes in the regime of the Nile River during the Holocene by investigating a laminated sediment sequence corresponding to the youngest sapropel layer (S1) from the Nile deep-sea fan, which provides a very detailed record of the AHP and its termination. The changes in river runoff and main sources of the river waters have been previously investigated using sediment cores (Krom et al., 2002; Revel et al., 2010; Marriner et al., 2012),

geomorphology (Adamson et al., 1980; Williams, 2009) and lake levels (Gasse, 2000; Stager et al., 2003; Garcin et al., 2009, 2012; Marshall et al., 2011). However, these reconstructions only provide a fragmentary and/or low-resolution picture of the changes in river regime that prevents their comparison and does not allow assessing the response of the Nile River system to changes in orbital configuration and in seasonality. We thus aim at providing an integrated reconstruction of changes in Nile River runoff and freshwater source at high temporal resolution during the past 9.5 kyr from a single sediment archive. This will help evaluating the impact and the response of the Nile River system to changes in orbital parameters as well as to more abrupt climatic events previously recognized in North Africa (Gasse, 2000; Thompson et al., 2002; Kim et al., 2007). Finally, we aim at evaluating the impact of changes in the hydrological regime of Nile River on the marine environment (especially on the bottom-water oxygenation).

## 2. Regional settings

The drainage area of the Nile River extends from $\sim 4°S$ to $\sim 30°N$ and from $20°E$ to $40°E$ and the river flows northward over a total length of over 6700 km (Fig. 1). The main stream integrates contributions from four main tributaries, which are from South to North: the White Nile, the Sobat, the Blue Nile and the Atbara (Fig. 1a and b). The White Nile originates from the equatorial
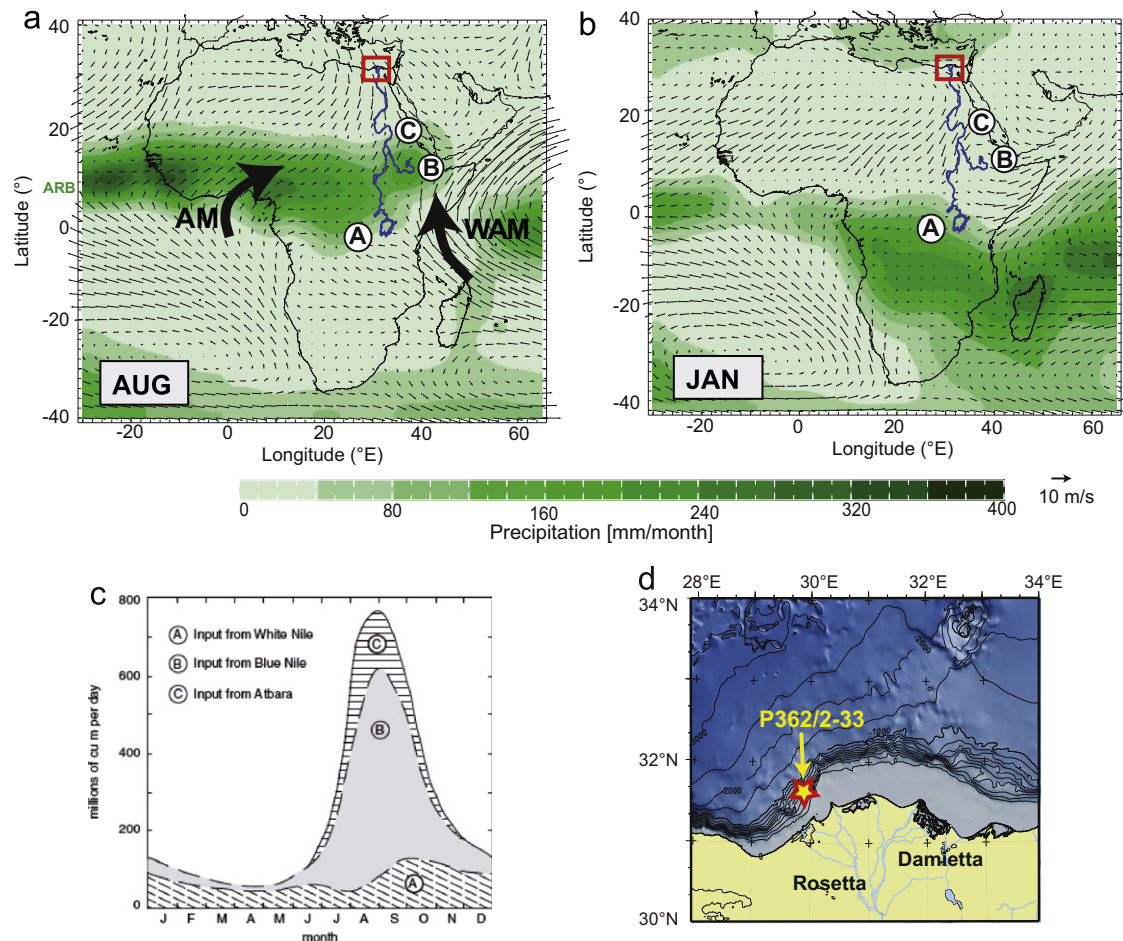


**Fig. 1.** Climate and regional settings. (a) and (b) Seasonal climatic patterns over Africa, with precipitation rates (green shading) and wind fields in August (a) and January (b). ARB: African Rain Belt, AM: African Monsoon, WAM: Western Asian Monsoon. A, B and C refer to the White Nile, Blue Nile and Atbara sources, respectively. (c) Relative contribution from the White Nile (A), the Blue Nile (B) and the Atbara (C) throughout the year. Redrawn from Williams et al. (2006), with permission from Elsevier. (d) Blow-up from the red squares in (a) and (b) and showing the location of core P362/2-33 on the Nile deep-sea fan (star). (For interpretation of the references to color in this figure legend, the reader is referred to the web version of this article.)

uplands of Uganda, Rwanda and Burundi, and in particular from the outflow of Lake Victoria and Lake Albert. The Sobat, the Blue Nile and the Atbara rivers originate from the Ethiopian Highlands. Prior to the construction of the Aswan Dam (which presently traps most of the particulate matter), the sedimentation on the Nile delta was largely controlled by seasonal variations in precipitation onto the Nile watershed. The White Nile and Sobat rivers contribute a relatively continuous amount of water throughout the year given that the wet season in the Equatorial upland region lasts for more than 8 months (Fig. 1a and b) (Nicholson, 2000). The Blue Nile and Atbara tributaries contribute large amounts of water in summer when the African Rain Belt migrates to its northernmost location (Fig. 1a). Most of the sediment transported by the Nile River originates from the marked summer floods of the Blue Nile and the Atbara Rivers (Adamson et al., 1980; Williams et al., 2006). Therefore, although the White Nile is responsible for a third of the annual flow of the Nile (and up to 80% in the drier months), it provides only about 3.5% of the annual sediment load (Fig. 1c). In contrast, the Blue Nile and Atbara together supply $\sim 65\%$ of the annual flow and 96.5% of the annual sediment load (Adamson et al., 1980). The Blue Nile and Atbara also run through mantle-derived volcanic rocks that are more susceptible to erosion than the crystalline basement of the White Nile catchment.

Eolian dust is deposited on the Nile Delta at a rate of 20–40 g m$^{-2}$ yr$^{-1}$ and mostly originates from North African sources and especially the Lybian desert (Herut et al., 2001; Prospero et al., 2002). This source is mainly active during the spring and is related to the North Atlantic Oscillation on interdecadal scale (Guerzoni et al., 1997; Moulin et al., 1997).

# 3. Material and methods

## 3.1. Sediment core P362/2-33

Marine sediment core P362/2-33 was recovered on the Nile deep-sea fan (31°40.51N; 29°45.00E) during R/V Poseidon cruise P362/2 in August 2008 (Fig. 1d) (Feseker et al., 2010). This 559-cm long gravity core consists of undisturbed laminated hemi-pelagic sediments of which the upper 40 cm show a gradual change from brownish to grayish color with yellowish oxidation spots and traces of bioturbation (Fig. 4). Faint laminations are observed between 75 and $\sim 105$ cm core depth within a layer of gray to green colored sediments. Well-preserved (sub)millimeter-scale laminations are observed below 140 cm core depth and consist of sediments alternating between dark-gray and light-gray colored layers and are similar to laminated sediments at around 2000 m water-depth on the Nile deep-sea fan (Ducassou et al., 2008; Revel et al., 2010). These laminations were interpreted as very dense suspension-rich (hyperpycnal) flows formed by reconcentration of particle-laden seasonal Nile flood plumes in the water column, which were subsequently deposited on the seafloor (Ducassou et al., 2008). In this interval, high amount of pyrite and an absence of benthic foraminifera were observed during sediment wet sieving (data not shown).

## 3.2. Methods

### 3.2.1. Core scanning

The bulk major element composition was measured throughout core P362/2-33 using an AavatechTM X-ray fluorescence (XRF) core scanner at the Institute of Geosciences of the University of Kiel (Germany). Non-destructive XRF core-scanning measurements were performed at 10, 30 and 50 kV in order to measure the relative content of elements ranging from aluminum

(Al) to barium (Ba) (Tjallingii et al., 2007). Measurements at 10 and 30 kV were acquired every 1 cm, whereas measurements at 50 kV were performed every 1 cm for the upper meter and every 2 cm for the remaining part of the core. Initially, the elemental composition obtained by XRF core-scanning is provided as count rates, which depend on elemental concentration but are also susceptible to down-core variations of physical properties and sample geometry (Tjallingii et al., 2007). Therefore, we will use log ratios of elemental count rates, which provide the most readily interpretable signals of relative changes in chemical composition free of constant-sum constraint (which is due to the fact that elements are de facto correlated to each other in compositional datasets) and minimize the effects of sample geometry and physical properties (Weltje and Tjallingii, 2008). The relationships between major elements were explored using principal component analyses (PCA), which was calculated using the freeware R (R Development Core Team, 2011) (Fig. 3a and b). The PCA is a multiple regression method that allows examining the statistical relationships between several variables (Everitt and Hothorn, 2006). In order to avoid the constant-sum constraint, we performed an R-mode PCA on the centered log-ratio correlation matrix (Kucera and Malmgren, 1998).

The volumetric low-field magnetic susceptibility measurements were performed every 1 cm on split half-sections of the core using the Geotek multi-sensor core-logger (MSCL). The magnetic susceptibility (reported in 10$^{-5}$ SI) was measured using a susceptibility meter Bartington MS2E mounted on the Geotek MSCL at the GEOMAR (Germany).

### 3.2.2. Elemental carbon and carbonate content analyses

Total organic carbon (TOC) and total calcium carbonate (CaCO$_3$) contents (in %) were measured every 5 cm for the uppermost meter and every 3 cm for the rest of the core using a Carlo Erba NA 1500 elemental analyzer at the GEOMAR. Accuracy and precision of the measurements were checked using replicate analysis of acetanilide ($C=71.09\%$) and of an internal standard. The total carbon (TC) content (%) was measured in duplicate using 3–20 mg of freeze-dried and ground sediment samples. The carbonates were then removed using a 0.25 M HCl solution and the TOC content was measured in duplicate using the decarbonated samples. The total inorganic carbon (TIC) content was estimated by the difference between TC and TOC and the CaCO$_3$ contents were calculated using the equation: CaCO$_3 =$ TIC $\times$ 8.33 (Verardo et al., 1990).

### 3.2.3. Grain-size distribution of the siliciclastic particles

The siliciclastic fraction of the sediments was isolated from the bulk sediment samples by removing subsequently the carbonates using a buffered acetic acid solution, the authigenic ferromanganese coatings using a hydroxylamine solution (Gutjahr et al., 2007) and the organic matter using concentrated hydrogen peroxide. In order to prevent the neoformation of particle aggregates, the residual samples were shortly boiled with a sodium pyrophosphate solution before measuring the grain-size distribution using a Coulter Laser Seizer (LS230) at the NIOZ (The Netherlands).

Statistically meaningful end-members (EMs) were calculated from the total set of grain-size measurements ($n=24$) using the end-member model algorithm (EMMA) of Weltje (1997). In this case, a three-EM model explains 99.5% of the total amount of variance (Fig. 3d). The small amount of samples used here might reach the limit of the statistical significance. Therefore, the EMMA was applied on the complete core as well as on the laminated part only and the similarity of the EMs obtained in both calculations attests the reliability of the modeling (not shown). The grain-size distribution obtained by EM modeling was used to separate the

siliciclastic fraction prior to analyzing the neodymium and strontium radioisotope signatures. The changes in proportion of the EMs were explored using log ratios in order to avoid the constant-sum constraint.

### 3.2.4. Radiogenic isotopes

The radiogenic isotope composition of neodymium (Nd) and strontium (Sr) was measured on the siliciclastic fraction of the sediments. Based on the results of the EMMA, the siliciclastic fraction was separated into three different grain-size fractions ($\leq 2\ \mu m$, $2-10\ \mu m$ and $\geq 10\ \mu m$) using a centrifuge. Centrifugation time was calculated using the freeware 'Sedicalc' (Krumm, 2006). Those fractions of about 0.05 g were totally dissolved using subsequently: (i) concentrated nitric and hydrofluoric acid and (ii) concentrated nitric, hydrofluoric and perchloric acids. Standard column-chromatography procedures were applied to separate and purify Nd and Sr (Cohen et al., 1988; Horwitz et al., 1992). The Nd and Sr isotope composition was measured on a Nu Instruments multi-collector inductively-coupled plasma mass spectrometer (MC-ICP-MS) at the GEOMAR. Blank levels were negligible for analyses of both radiogenic Nd and Sr isotopes ($\leq 0.3$ ng for Nd and $\leq 3.4$ ng for Sr). The isotope results were normalized to the accepted values of the JNdi standard for Nd ($^{143}Nd/^{144}Nd = 0.512115$) and of the NBS SRM 987 standard for Sr ($^{87}Sr/^{86}Sr = 0.710245$) to account for analytical shift. The Nd isotope ratios are reported as $\epsilon Nd$, which is the corrected $^{143}Nd/^{144}Nd$ ratio normalized to CHUR ($^{143}Nd/^{144}Nd = 0.512638$, Jacobsen and Wasserburg, 1980) and multiplied by 10,000. External reproducibility was first estimated by repeated measurements of in-house SPC and SPEX standards for Nd and the AA standard for Sr, and the isotope ratios are reported with $2\sigma$ uncertainties of $\pm 0.52\epsilon Nd$ units ($\pm 30$ ppm, $n = 10$) for Nd and $\pm 0.00005$ ($\pm 65$ ppm, $n = 20$) for Sr. External reproducibility was further assessed by repeated measurements of JNdi standard for Nd and NBS SRM 987 standard for Sr, and yielded $2\sigma$ uncertainties of $\pm 0.3\epsilon Nd$ units ($\pm 30$ ppm, $n = 10$) and $\pm 0.000025$ ($\pm 25$ ppm, $n = 20$) for Sr. It should be noted that the uncertainties reported here are the highest obtained, i.e. for the samples and standards with the lowest concentrations (50 ppb for Nd and 25 ppb for Sr).

### 4. Age model

The chronology of the sediment core was determined by $^{14}C$ measurements of planktonic foraminifera shells (*Globigerinoides ruber* and *Globigerina bulloides*). Approximately 10 mg of hand-picked shells collected from 14 samples was analyzed at the Leibniz-Laboratory for Radiometric Dating and Stable Isotope Research of the University of Kiel (Germany) (Table 1). The uppermost 3 cm of the core contains steamboat cinder remnants indicating that these sediments were deposited between AD1800 and AD1950 (i.e., $75 \pm 75$ yr BP) and the sediments at the bottom of the core were dated at $\sim 9000\ ^{14}C$ yr BP. The ages younger than 6500 $^{14}C$ yrs were corrected for the average reservoir age of seawater (400 yr), which is in agreement with the age of $370 \pm 40$ yr obtained for a pre-bomb shell of *Muricopsis trunculus* collected in Alexandria (Goiran, 2001). Ages between 9200 and 6500 $^{14}C$ yr were corrected using a reservoir age of $515 \pm 20$ yr determined by Facorellis and Maniatis (1998) for the early Holocene in the Eastern Mediterranean. Higher reservoir ages at this time are probably associated with the large amount of $^{14}C$-depleted freshwater delivered by the Nile River during the African Humid Period (Siani et al., 2001). Overlapping and partly reversed ages occur at 400 and 557 cm (Fig. 2), which are probably related to the very high sedimentation rates of 60–650 cm/ka in the laminated part of the core. In order to provide a continuous

**Table 1**

Age model for core P362/2-33 based on 14 $^{14}C$ ages. All $^{14}C$ ages were obtained on mixed planktonic foraminifera (*G. ruber* and *G. bulloides*). The uncertainties on the ages are reported as $2\sigma$. Ages marked with an asterisk (∗) were corrected for a marine reservoir age of 400 yr (Goiran, 2001) and all other ages were corrected for 515 yr (Facorellis and Maniatis, 1998; Siani et al., 2001) (see text for details). All reservoir-corrected $^{14}C$ ages were then adjusted on the calendar scale using the online freeware Calib 6.0 (Stuiver et al., 2005) and the Marine09 curve (Hughen et al., 2004; Reimer et al., 2009). Numbers in bracket in the calibrated age range column represent the probability areas. Mean $^{14}C$ ages and their uncertainty were rounded to the lower or the upper 5 yr.

| Depth (cm) | $^{14}C$ age (yr) | Reserv.-corr. $^{14}C$ age (yr) | Cal. $^{14}C$ age range (cal. yr) | Mean cal. $^{14}C$ age (cal. yr) |
|---|---|---|---|---|
| $30 \pm 0.5$ | $3825 \pm 30$ | $3425^*$ | 3676–3876 | **$3775 \pm 100$** |
| $50 \pm 0.5$ | $5695 \pm 30$ | $5295^*$ | 5993–6193 | **$6110 \pm 100$** |
| $75 \pm 0.5$ | $6855 \pm 35$ | 6340 | 7141–7347 | **$7325 \pm 105$** |
| $100 \pm 0.5$ | $7340 \pm 45$ | 6825 | 7558–7778 | **$7655 \pm 110$** |
| $151.5 \pm 2.5$ | $7920 \pm 45$ | 7405 | 8123–8363 | **$8240 \pm 120$** |
| $200 \pm 0.5$ | $8115 \pm 55$ | 7600 | 8313–8565 | **$8430 \pm 125$** |
| $251.5 \pm 2.5$ | $8360 \pm 40$ | 7845 | 8574–8928 | **$8725 \pm 180$** |
| $300 \pm 0.5$ | $8375 \pm 60$ | 7860 | 8567–8964 | **$8750 \pm 200$** |
| $327 \pm 3$ | $8495 \pm 35$ | 7980 | 8744–9058 | **$8925 \pm 160$** |
| $399 \pm 1$ | $8440 \pm 45$ | 7925 | 8646–8991 | **$8845 \pm 175$** |
| $463 \pm 2$ | $8680 \pm 40$ | 8165 | 9007–9309 | **$9165 \pm 150$** |
| $499 \pm 1$ | $8805 \pm 45$ | 8290 | 9164–9166 (0.002) 9173–9456 (0.998) | **$9330 \pm 145$** |
| $547 \pm 3$ | $9010 \pm 35$ | 8495 | 9428–9629 | **$9515 \pm 100$** |
| $557 \pm 1$ | $8780 \pm 50$ | 8265 | 9122–9437 | **$9300 \pm 160$** |

chronostratigraphy, a best-fit model was calculated for the lowermost 200 cm of the core using the Bayesian approach developed by Blaauw and Christen (2011) and implemented in the freeware 'Bacon' (Fig. 2). All ages were converted into the calendar age scale (ka BP) using the Marine09 curve (Reimer et al., 2009) implemented in the software Calib 6.0 (Stuiver et al., 2005). Sedimentation rates vary from $\sim 650$ cm/kyr in the lower part of the core to $\sim 8$ cm/kyr in the upper part (Fig. 2).

## 5. Results and interpretations

### 5.1. Changes in sediment composition: sediment supply and diagenetic modifications

According to the results of the PCA, we show the loadings of the elements on PC1, PC2 and PC3 as these three principal components (PCs) explain more than 80% of the total variance (Fig. 3a and b). The first striking characteristic of the dataset is the strong anti-correlation of the elements calcium–strontium–manganese (Ca–Sr–Mn) to the other elements on PC1 (Fig. 3a). On PC2 and PC3, Mn is anti-correlated to Ca–Sr, which suggests that Mn has a distinct behavior (Fig. 3a and b). The second important characteristic is the existence of two clusters for the 'terrigenous' elements that are anti-correlated on PC2: a potassium–aluminum–silicon (K–Al–Si) cluster and a zirconium–titanium–iron–rubidium (Zr–Ti–Fe–Rb) cluster (Fig. 3a). This may either be related to different sediment sources and sorting or different sensitivities toward weathering. The elements sulfur (S), bromine (Br), chlorine (Cl) and barium (Ba) are close to the Zr–Ti–Fe–Rb cluster on PC1 and PC2 (Fig. 3a). On PC3, Ba and Cl are strongly anti-correlated and S is close to Zr (Fig. 3b).

Based on these results, we selected a number of elemental ratios and geophysical parameters to reconstruct the down-core changes in sediment composition (Fig. 4). First, we used the magnetic susceptibility (MS), the Mn/Al and Ba/Al ratios, as well as the TOC contents to characterize the relationships between
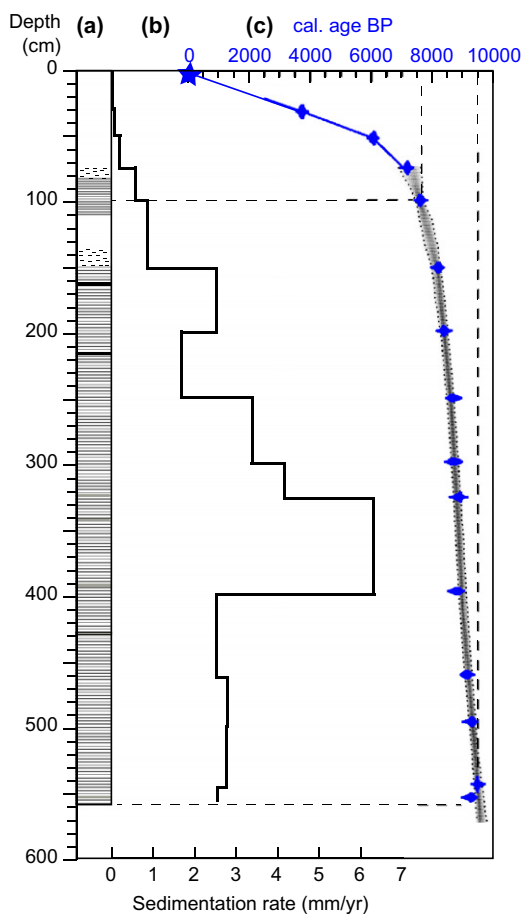
**Fig. 2.** Lithology and age model for core P362/2-33. (a) Log of lithologic changes against depth, with horizontal lines representing the laminations and dashed horizontal lines representing faint laminations. Thick dark and gray layers refer to thicker dark-colored or light-color layers. (b) Changes in sedimentation rates along depth. (c) Violin plot of the calibrated $^{14}$C ages, which gives an estimation of the statistical density of the age-depth relationship for each age. The gray shading represents the age-model obtained by a Bayesian approach that was realized (as well as the plot) using the Bacon software (Blaauw and Christen, 2011). The star at the top of the core represents the estimated age of remnant steamboat cinders.

sediment composition, lithology and diagenesis (Fig. 4a–d). The MS gives an estimation of the amount of iron oxides, in particular of magnetite ($Fe_3O_4$) in the sediments, which originate from continental surface erosion and can be depleted during early diagenesis (Jørgensen and Kasten, 2006). The Mn/Al and Ba/Al ratios are used to identify layers of diagenetic accumulation of Mn and Ba (Reitz et al., 2006) and Ba/Al is also related to changes in export production (Mercone et al., 2000). The Mn/Al and Ba/Al ratios have been widely used to identify the extent of the sapropel layers and the occurrence of burn-down processes (De Lange et al., 2008). The downward-migration of the redox front after the sapropel deposition might indeed lead to complete removal of the TOC in the upper part of the sapropel layers, whereas Ba/Al remains unaffected (Froelich et al., 1979). In core P362/2-33, enrichments in Mn/Al and Ba/Al are observed in the upper 25 cm (at 5 and 20 cm) and are accompanied by high values in the MS ($200 \times 10^{-5}$ at $\sim$10 cm) and in the TOC content. This probably reflects the on-going reduction of manganese and iron oxides during the microbial degradation of organic matter (Jørgensen and Kasten, 2006). The peak in Mn/Al and Ba/Al at 25 cm most likely indicates the location of the present redox front, where upward-migrating $Ba^{2+}$ and downward-migrating $Mn^{2+}$ did precipitate. The laminated interval is characterized by low MS values ($\leq 50 \times 10^{-5}$ SI), low Mn/Al ratios and higher TOC content

($\sim$1.1%). The Ba/Al ratio increases upwards throughout the laminated interval and is high between 60 and 90 cm. Both the Ba/Al ratio and the TOC content start to decrease at 80 cm (which is the last occurrence of laminations) but show a major decrease at 60 cm. This suggests that burn-down processes were of minor influence in core P362/2-33 on the TOC content and that the sapropel layer extends up to 60 cm. The absence of extensive burn-down processes was already observed for cores with high accumulation rates in this region (Mercone et al., 2000).

The changes in marine/terrigenous material and within the detrital material are investigated by comparing the Ti/Ca and Ti/Al ratios (Fig. 4e and f). These ratios show a relatively similar pattern, with higher values in the sapropel layer, lower values between 40 and 20 cm and high values in the upper 10 cm. The enrichment of the sapropelic sediments in Ti most probably indicates a higher contribution by Nile particulate matter (Krom et al., 1999). The Ti/Ca and Ti/Al ratios decrease gradually between 100 and 25 cm, which suggest a progressive reduction of river input.

## 5.2. Grain-size distribution: sources and transportation mechanisms of terrigenous particles

Terrigenous particles deposited in marine sediments generally originate from distinct sources and underwent different modes of transport, which are characterized by specific grain-size distributions (Weltje and Prins, 2003). For our dataset, a three end-member (EM) model explained about 99.5% of the total variance and allowed the definition of a coarse multimodal EM (EM1) and two bimodal hemipelagic EMs (EM2 and EM3) (Fig. 3d). The poorly sorted grain-size distribution of EM1 ranges from 0.1 to 200 µm with two main modes between 15 and 30 µm. The grain-size distributions of the two hemipelagic EM2 and EM3 range between 0.1 and $\sim$40 µm, with distinct modal grain-sizes of 3–4 µm and 2 µm, respectively. The grain-size distribution of the EMs matches that of present-day fluvial and eolian material collected in the region. Like the EM1, the grain-size distributions of Mediterranean aerosols range from 1 to 100 µm and are typically poorly sorted with a modal size of 10–30 µm (Guerzoni et al., 1997). Like the hemipelagic EM2 and EM3, the Nile River particles fall into the mud size-fraction, with particles originating from the Blue Nile being generally coarser than those originating from the White Nile (Billi and el Badri Ali, 2010). Coarser particles are indeed produced by the intense erosion occurring during summer floods in the erodible volcanic watershed of the Blue Nile. In contrast, the year-round precipitation pattern at the source of the White Nile enables the development of a vegetation cover that tends to protect the more resistant crystalline basement from erosion. Furthermore, the sediment load of the White Nile is filtered when passing into the large swamps of the Sudd, before the convergence with the Blue Nile and Atbara Rivers (Williams et al., 2006). These climatic, geographic and geologic differences also explain that most sediment presently delivered to the margin originates from the Blue Nile drainage area (Adamson et al., 1980). Therefore, we assume that EM2 is enriched in coarser particles originating from floods of the Blue Nile River as compared to EM3.

In order to further assess the provenance of the EMs, we separated four samples into three grain-size fractions ($\leq 2$ µm, 2–10 µm and $\geq 10$ µm) and measured their Nd and Sr radio-isotope composition (Table 2 and Figs. 5 and 6). The samples collected at 30, 85 and 221 cm depth contain dominant proportions of EM1, EM3 and EM2, respectively (Fig. 5). The sample collected at the core-top (0 cm depth) contains an equal proportion of EM2 and EM3. The EM2 and EM3 have $\epsilon$Nd values that are not significantly different and comprised between $\sim$0 and
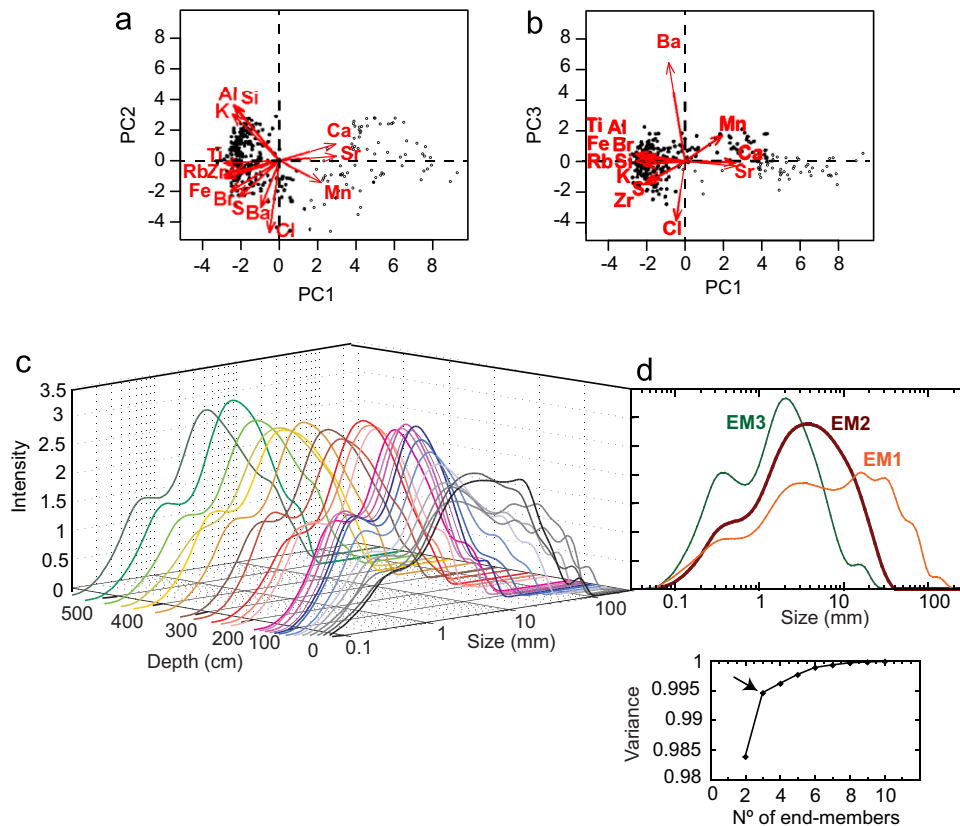
**Fig. 3.** Results of statistical analyses performed on the bulk elemental contents measured using XRF-core scanning (a, b) and on the grain-size distribution of the siliciclastic fraction (c, d). Principal component analyses for major and trace elements: (a) Loadings of each element and scores of the samples along the two first principal components, PC1 and PC2, which represent respectively ∼ 62% and ∼ 18% of the total variance. (b) Loadings and scores along PC1 and PC3, the latter representing ∼ 7% of the total variance. End-member modeling analyses (EMMA) for the grain-size analyses of the siliciclastic fraction. (a) 3D-plot of the grain-size distribution for each sample along depth. (b) Result of the EMMA (Weltje, 1997), with the grain-size distribution of three first end-members (EM1 in orange, EM2 in brown and EM3 in green) that explain more than 0.995% of the total variance (subplot below). (For interpretation of the references to color in this figure legend, the reader is referred to the web version of this article.)

∼ −4 εNd units but these EMs can be clearly distinguished by their $^{87}Sr/^{86}Sr$ signatures of ∼ 0.710 and ∼ 0.707, respectively (Table 2). When compared to the radiogenic isotope composition of present-day Nile and dust particles (Fig. 6), the radiogenic isotope compositions of EM2 fall close to those of particulate matter from the Blue Nile and Atbara River. The radiogenic isotope compositions of EM3 fall between those of the Blue Nile and the White Nile (Padoan et al., 2011). The EM1 has the least radiogenic εNd (−7.99 ± 0.52) and most radiogenic $^{87}Sr/^{86}Sr$ values (∼ 0.712) falling between the White Nile and the Saharan/Lybian dust end-members (Revel et al., 2010). Therefore, the radiogenic isotope signatures of the EMs support the interpretation that EM1 is mostly composed of dust-borne particles and that EM2 is enriched in particles originating from Blue Nile floods as compared to EM3, which probably represents the background sediment load of the Nile River.

Down-core variations in grain-size distribution are compared to changes in the relative proportion of the three EMs (Fig. 5a and b). The EM1/(EM2+EM3) ratio is used to estimate the variations of eolian versus fluvial input to the sediments (Fig. 5c). The EM2/EM3 ratio is used to estimate the changes in relative intensity of the Blue Nile discharge (Fig. 5c). Four depth intervals can be distinguished: (i) from 560 to 200 cm, EM2 dominates and indicates a major input from the Blue Nile; (ii) from 200 to 60 cm, EM3 is the most abundant and suggests a relatively low Blue Nile discharge and perhaps a larger contribution from the White Nile; (iii) from 60 to 15 cm, EM1 is the most abundant and indicates higher contribution of eolian material to the siliciclastic fraction of the sediments; (iv)

the upper 15 cm, where EM1 and EM2 prevail, which suggest mixed eolian and fluvial input at comparable amounts.

### 5.3. Fluvial control on sedimentation

At the site of core P362/2-33, the changes in sediment composition and accumulation rate have directly been controlled by changes in fluvial source and discharge. Changes in terrigenous/marine contributions as indicated by the Ti/Ca ratio are similar to changes in the fluvial/eolian contributions that are monitored by the EM1/(EM2+EM3) ratio (Fig. 7a–c). Between 9.5 and 7.3 ka BP, high terrigenous contribution are indicated by high Ti/Ca ratio and are predominantly of fluvial origin as suggested by the low amount of EM1. From 7.3 to 3.7 ka BP, the decrease in Ti/Ca ratio suggests that the proportion of terrigenous material in the sediments decreased, whereas the proportion in eolian-derived EM1 gradually increased. These decreases in fluvial/eolian and terrigenous/marine contributions to the sediments are likely related to a decrease in fluvial discharge as shown by the decrease in the level of the Nile River between 8 and 4 ka BP previously observed by Williams and Adamson (1974). The proportion of terrigenous particles in the sediments and the fluvial contribution both increase again from 4 ka until 1 ka BP.

The synchronous change between 9.5 and 7 ka BP in both the EM2/EM3 ratio (Fig. 7e) and the sedimentation rates (Fig. 7f) suggest that during periods of high fluvial discharge, the sediment supply to the margin has been mainly controlled by switches in the fluvial source. Indeed, the abrupt reduction in the proportion
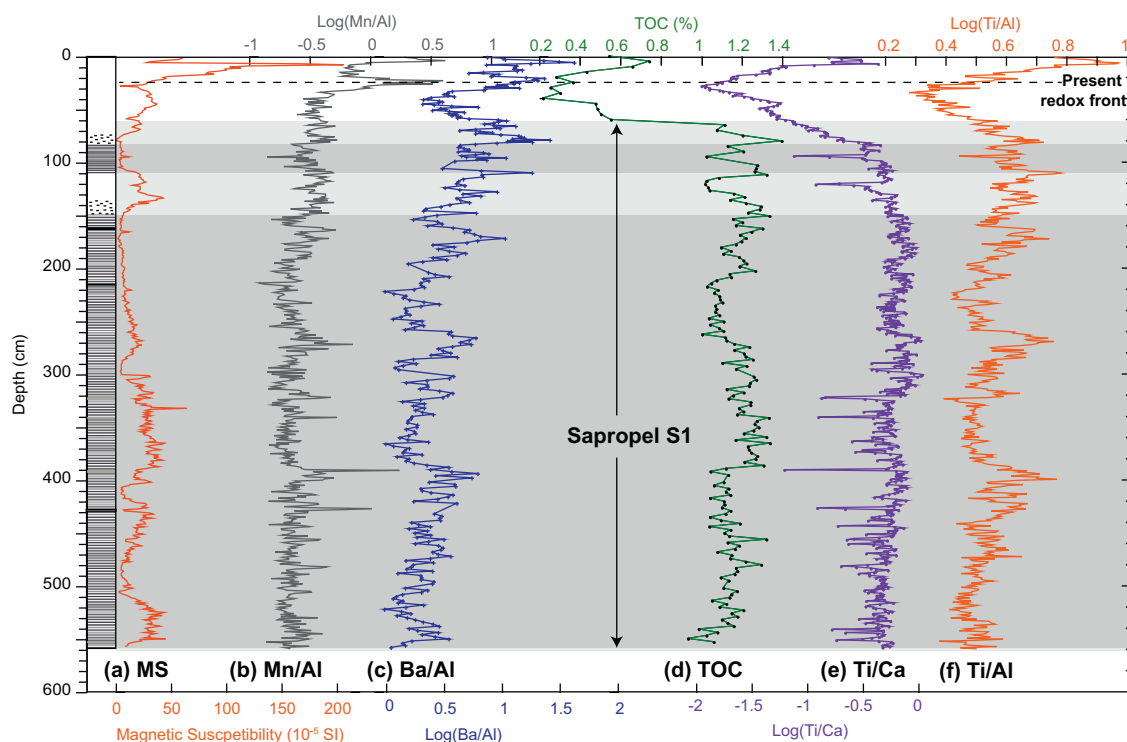
**Fig. 4.** Down-core profiles of various geochemical and geophysical parameters. Left: Log of lithological changes (see legend in caption of Fig. 2). (a) Magnetic susceptibility and (d) total organic carbon (TOC) content. Logarithms of elemental ratios: (b) manganese/aluminum (Mn/Al), (c) barium/aluminum (Ba/Al), (e) titanium/calcium (Ti/Ca) and (f) titanium/aluminum (Ti/Al). The location of the present redox front is indicated as a dashed line and the depth extend of the sapropel layer is indicated by the vertical arrows. The laminated intervals are also underlined by a gray shading.

**Table 2**
Radiogenic Nd and Sr isotope composition of grain-size fractions. All numbers are reported with $2\sigma$ uncertainty.

| Fraction | Depth (cm) | $^{143}Nd/^{144}Nd$ | $\epsilon Nd$ | $2\sigma$ | $^{87}Sr/^{86}Sr$ | $2\sigma$ |
|---|---|---|---|---|---|---|
| EM3 ($\leq 2\ \mu m$) | 0 | 0.512604 | −0.67 | 0.52 | 0.710261 | 0.000046 |
| | 85 | 0.512444 | −3.79 | 0.52 | 0.709444 | 0.000046 |
| | 221 | 0.512457 | −3.52 | 0.52 | 0.709974 | 0.000046 |
| EM2 | 0 | 0.512549 | −1.74 | 0.52 | 0.707660 | 0.000046 |
| ($2-10\ \mu m$) | 221 | 0.512457 | −3.53 | 0.52 | 0.707346 | 0.000012 |
| EM1 ($\geq 10\ \mu m$) | 30 | 0.512223 | −7.99 | 0.52 | 0.712723 | 0.000016 |

of coarse sediments originating from the Blue Nile between 8.5 and 7.3 ka BP as indicated by the decrease in EM2/EM3 ratio (Fig. 7e) is synchronous with a rapid decrease in sedimentation rate (Fig. 7f). The Blue Nile was obviously the principal contributor of fluvial sediments from 9.5 to 8.5 ka BP, after which its influence decreased abruptly to reach a minimum at 7.3 ka BP. The relative contribution from the Blue Nile remained low until ∼ 6 ka BP while the relative contribution from White Nile was perhaps enhanced. Interestingly, the increase in proportion of material from the Blue Nile between 3 and 1 ka BP was not accompanied by an increase in sedimentation rate. These observations suggest that switches in the fluvial source areas controlled the sedimentation supply only during periods of high fluvial input, such as the AHP. Our reconstructed changes in relative intensity of the Blue Nile discharge to the Nile deep-sea fan agree with previous studies. Higher Blue Nile sediment flux during the early and late Holocene was estimated from marine sediments from the Levantine Basin based on their Sr isotopic signature (Box et al., 2011) (Fig. 7d). Enhanced supply of material

from the White Nile between 8 and 6 ka was also hypothesized from Eastern Mediterranean sediment cores (Revel et al., 2010; Box et al., 2011). The Late Holocene increase in Blue Nile contribution was observed using Sr isotopic signature of sediments from the eastern Nile Delta (Krom et al., 2002) (Fig. 7e).

## 6. Climatic implications

### 6.1. Influence of low-latitude insolation

The changes in fluvial discharge and source areas as recorded by core P362/2-33 have apparently been primarily controlled by summer and spring/autumn low-latitude insolation changes. The river runoff gradually decreased between 8 and 4 ka BP (Fig. 8b and c) following the summer insolation at 20°N (Fig. 8a). Precession-forced insolation changes at low latitudes are the principal control on the position and strength of monsoonal systems and related precipitation belts (Gasse, 2000; Haug et al., 2001; Wang et al., 2001; Tjallingii et al., 2008). We therefore postulate that the total runoff of the Nile has mainly been controlled by changes in precipitation within the overall drainage area, which was related to a contraction of the African Rain Belt around the Equator following the changes in summer insolation after 10 ka BP (Gasse, 2000; Collins et al., 2011).

The changes in relative intensity of the Blue Nile discharge have mainly been driven by variations in spring/autumn low-latitude insolation (Fig. 8e and f). Sediment supply by the Blue Nile was enhanced during the early and late Holocene at times of higher spring insolation, and was reduced between 8 and 4 ka at times of low spring insolation and high autumn insolation (Fig. 8e and f). Additionally, periods of enhanced supply from the Blue Nile positively correlate with high sedimentation rates during the early Holocene, but this is not observed during the late Holocene
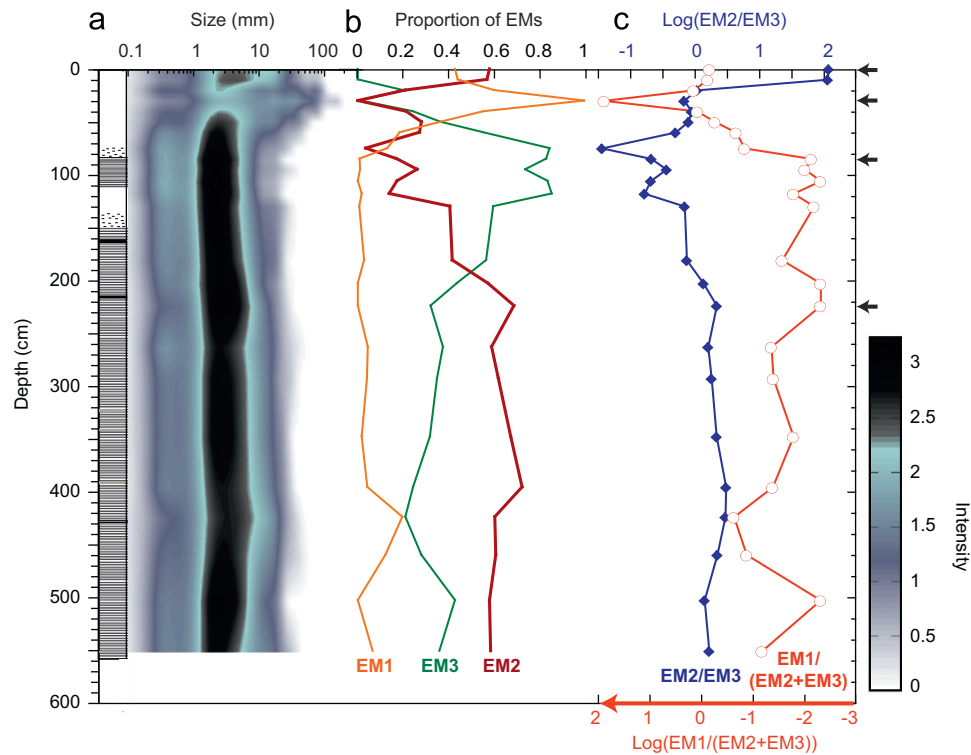
**Fig. 5.** Down-core profiles of the grain-size distribution and proportion of the grain-size end-members. Left: Log of lithological changes (see legend in the caption of Fig. 2). (a) Contour plot of the total grain-size distribution, with the gray scale indicating the relative abundance of a grain-size fraction (see key at the right of the plot). (b) Changes in the relative proportion of each end-member (EM1 in orange, EM2 in brown and EM3 in green). (d) Down-core variations of the EM1/(EM2+EM3) (on an inverted scale) and EM2/EM3 ratios, which are used to trace the fluvial versus eolian input and the relative intensity of the Blue Nile discharge, respectively (see text for more details). Arrows at the right of the plot indicate the location of the samples that were separated in different grain-size fractions (see Table 2). (For interpretation of the references to color in this figure legend, the reader is referred to the web version of this article.)
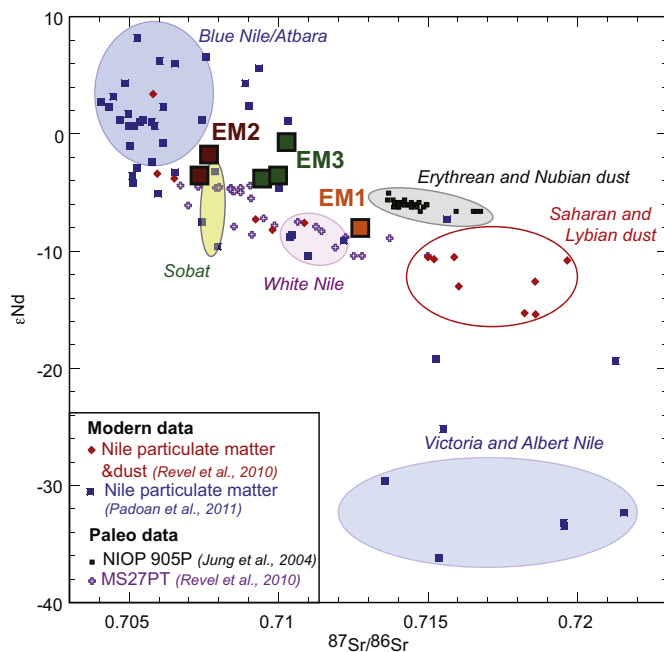


**Fig. 6.** Neodymium (Nd) and strontium (Sr) radioisotope signature for the three grain-size end-members (EM1 in orange, EM2 in brown and EM3 in green) as compared to the present-day or past signature of Nile suspended material (red diamonds and purple crosses: Revel et al., 2010; blue squares: Padoan et al., 2011) and regional aerosols (black squares: Jung et al., 2004; Revel et al., 2010). The error bars are smaller than the symbols for EM1, EM2 and EM3. (For interpretation of the references to color in this figure legend, the reader is referred to the web version of this article.)

(Fig. 8f and g). These changes are best explained by shifts in the seasonal distribution of insolation following the precession of the equinoxes during the Holocene (Fig. 8d) (Marzin and Braconnot, 2009).

Presently, most of the Blue Nile runoff occurs during summer and accounts for ~50% of the annual Nile runoff, whereas the White Nile runoff is higher during the autumn and accounts for ~30% of the annual Nile runoff (Fig. 1) (Williams et al., 2006). In addition, most of the sediment load of the Nile today is provided by the Blue Nile (~70%), whereas the contribution of the White Nile is negligible (~4%). This predominance of supply by the Blue Nile is largely related to the current orbital configuration, with the peak of insolation occurring during the boreal summer solstice (Fig. 8d). During the early Holocene the peak of insolation also occurred during the summer solstice but the summer insolation in the northern Hemisphere tropics was enhanced by ~10% compared to today (Fig. 8a). Higher summer insolation most likely enhanced the precipitation in the source area of the Blue Nile and lead to higher runoff and erosion in the Blue Nile watershed (Fig. 8g). Elevated lake levels were observed at the source of the Blue Nile during the early Holocene and were also related to an increased summer insolation (Gasse, 2000; Marshall et al., 2011; Garcin et al., 2012). At 6 ka BP, summer insolation in the North Hemisphere tropics was also higher relative to today (by ~6%) but was shifted toward the autumn equinox. We speculate that the decrease in summer insolation and the increase in autumn insolation led to a decrease in relative intensity of the Blue Nile discharge and perhaps to a relative increase in White Nile runoff (which occurs today mostly in autumn). Changes in lake levels in the African equatorial band have been related to changes in summer and spring insolation before (Garcin et al.,
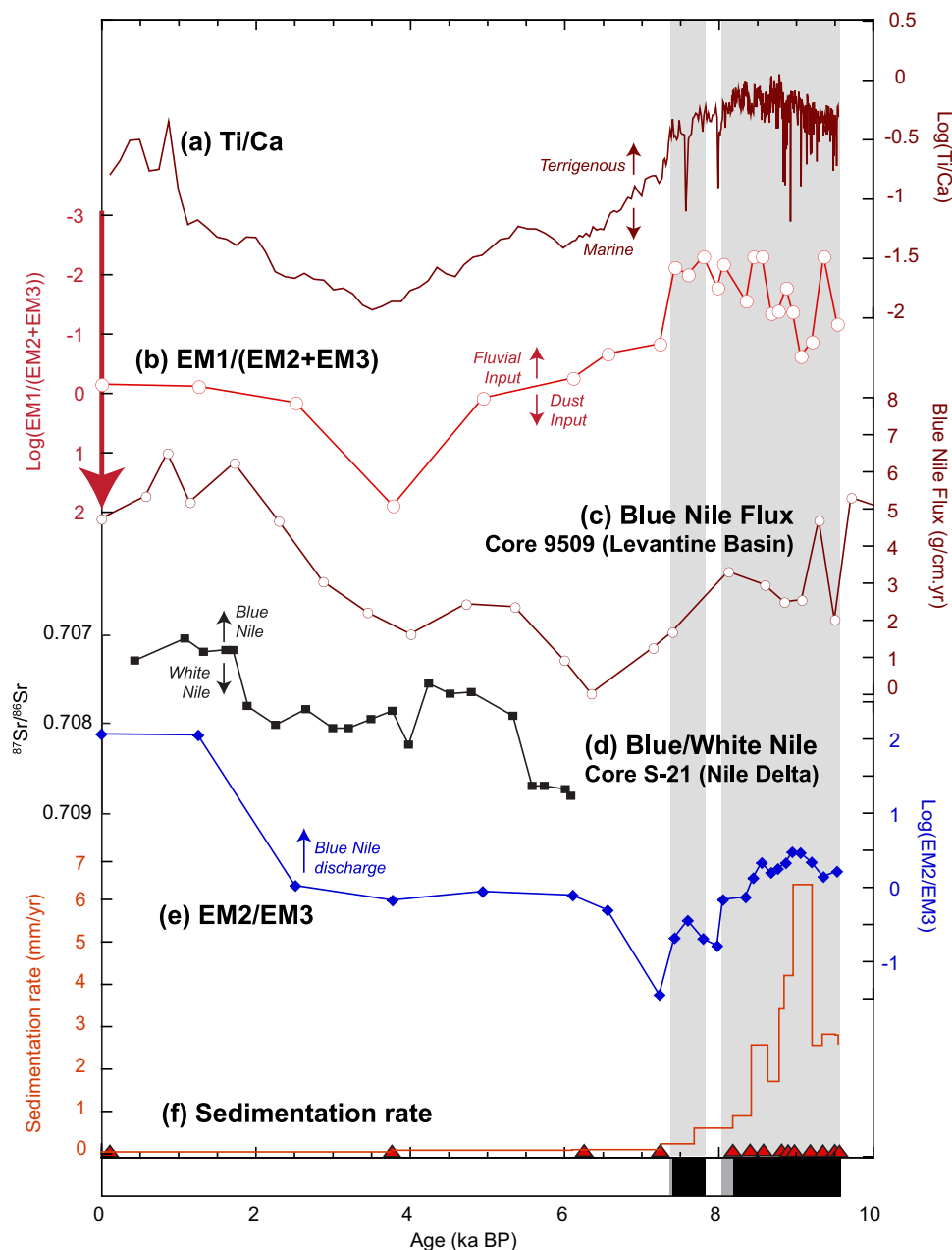
**Fig. 7.** Time variations in elemental content, grain-size distribution and sedimentation rate, as compared to other regional records. (a) Ti/Ca ratio, which is a tracer for marine versus terrigenous sedimentation. (b) EM1/(EM2+EM3) ratio (on an inverted scale), which provides a reconstruction of the fluvial/eolian contribution to the terrigenous fraction. (c) Flux of sediments originating from the Blue Nile and deposited in the Levantine Basin, as reconstructed from their radioisotope signature (Box et al., 2011). (d) $^{86}Sr/^{87}Sr$ composition for Nile Delta sediments that provide an estimation of the Blue Nile/White Nile contribution (Krom et al., 2002). (e) EM2/EM3 ratio, which traces the relative intensity of the Blue Nile discharge. (f) Sedimentation rates. The red triangles at the bottom of the panel represents the $^{14}C$-dated points, the black boxes and gray underlines represent the laminated intervals and the gray boxes represent the faintly laminated intervals. (For interpretation of the references to color in this figure legend, the reader is referred to the web version of this article.)

2009; Verschuren et al., 2009) and Lake Victoria, which is located at the source of the White Nile, had a high stand between 7.8 and 5.8 ka BP (Stager et al., 2003). The decrease in autumn insolation and the shift of the insolation peak toward the summer during the Late Holocene (i.e., between 4 and 0 ka BP) probably favored runoff from the Blue Nile, but the decrease in summer insolation most likely reduced the precipitation and erosion in the whole Nile drainage basin. Higher runoff and erosion were also observed in the Lake Tana basin (at the source of the Blue Nile) and were interpreted to result from higher seasonal rainfalls and enhanced catchment instability due to the recession of the vegetation cover (Marshall et al., 2011).

### 6.1.1. Millennial-scale climatic fluctuations: influence of high latitude climate?

The long-term and gradual changes observed and discussed previously were accelerated during a short-term event at 8.5–7.3 ka BP characterized by an abrupt decrease in contributions from the Blue Nile and a decrease in sedimentation rate at ~8.5 ka BP (Fig. 8f and g). Such a decrease in delivery of material from the Blue Nile was also deduced from geochemical analyses in a nearby core (Revel et al., 2010). Low-stands were observed for the same period of time in the Lake Tana and Lake Turkana records, which are located at the source of the Blue Nile (Marshall et al., 2011; Garcin et al., 2012). There is growing evidence that a
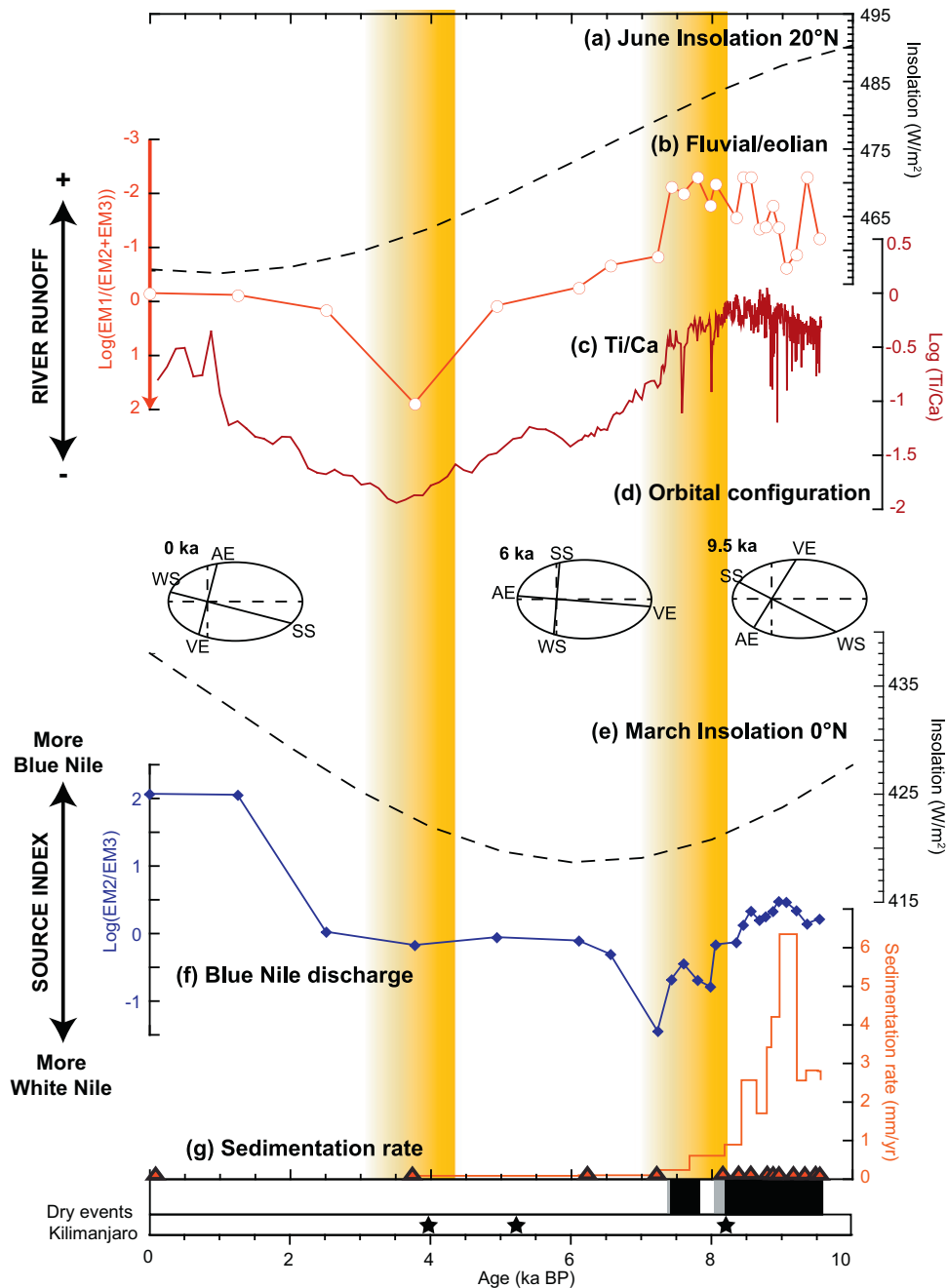
**Fig. 8.** Changes in sediment and fluvial dynamics as compared to the orbital and climatic context. (a) Summer (June) insolation at 20°N (Laskar et al., 2004). (b, c) Reconstruction of changes in Nile runoff using the EM1/(EM2+EM3) ratio (b) and the Ti/Ca ratio (c). (d) Changes in the orbital configuration following the precession of the equinoxes at 9.5, 6 and 0 ka (Marzin and Braconnot, 2009). (e) Spring (March) insolation at the Equator (Laskar et al., 2004). (f) Reconstruction of the changes in relative intensity of the Blue Nile discharge using the EM2/EM3 ratio. (h) Sedimentation rate. Red triangles at the bottom of the figure indicate the ^{14}C-dated points, black and gray boxes in the lower panel indicate the laminated and faintly-laminated intervals. The stars indicate dry events as recorded in an ice core from Kilimanjaro (Thompson et al., 2002). The yellow underlines indicate the occurrence of abrupt and short-term changes. (For interpretation of the references to color in this figure legend, the reader is referred to the web version of this article.)

large-scale hydrological perturbation occurred in equatorial and tropical Africa around 8.5 ka BP, which was characterized by low-stands in most lake records from northern Africa (Gasse, 2000). Additional evidence for a dry event around 8.5 ka BP was deduced from an increase in wind-blown deposits recorded by ice cores on the Kilimanjaro (Thompson et al., 2002). However, it is still debated whether this event resulted from meridional teleconnec-tions with a contemporaneous freshwater release in the North Atlantic that was linked to the abrupt cooling event observed in the Greenland ice-sheets at 8.2 ka BP (Alley et al., 1997). Rapid

drainage of Lakes Agassiz and Ojibway through the Hudson Strait occurred between 8.56 and 8.42 ka BP and the resulting sea-level rise has been dated at 8.45 ka BP (Hillaire-Marcel et al., 2007; Hijma and Cohen, 2010). It has been speculated that the reduction of the Atlantic meridional overturning circulation resulting from the freshwater release may have induced anomalous cooling events off northern Africa (such as the one observed at 8.5 ka BP off the coast of Morocco, Kim et al., 2007) and potentially triggered arid events in western Africa (deMenocal et al., 2000b; Renssen et al., 2007; Tjallingii et al., 2008). Conversely, the early

occurrence of the North African event, which has consistently been dated between 8.6 and 8.4 ka BP, led other authors to propose that the large hydrological change in low latitudes was a potential trigger for the 8.2 ka cooling event (Shanahan et al., 2007; Marshall et al., 2011). Our record shows a disruption of the AHP at 8.5 ka but does not provide any further support in favor of any of these scenarios.

Another remarkable climatic event of our record is the highly arid period between 4.3 and 3.7 ka BP, which represents a culmination in the gradual development of arid conditions in the drainage area of the Nile River. This event was characterized by a marked increase in dust contribution and by a slight decrease in relative intensity of the Blue Nile discharge (Fig. 8b, c and f). Many terrestrial records in North Africa depict the existence of a short-lived arid period centered at ∼ 4 ka BP, such as indicated by low lake levels (e.g., Gasse, 2000), enhanced dust deposition in Kilimanjaro ice cores and in the Gulf of Oman (Cullen et al., 2000; Thompson et al., 2002) and the cessation of runoff in the Wadi Howar river system, which was a major tributary of the Nile River during the AHP (Pachur and Kröpelin, 1987). A growing number of studies have reported a short period of intense drought occurring as the apex of a gradual aridification. For instance, the decrease in runoff to the Lake Tana Basin (Marshall et al., 2011), the development of aridification on the Somalian coast (Jung et al., 2004) and the vegetation transition at Lake Yoa (Kröpelin et al., 2008) all took place between 6.5 and 4.2 ka BP. The mechanisms underlying this drought event are highly complex and may involve meridional teleconnection such as those discussed for the 8.2 ka event (deMenocal et al., 2000b; Wang et al., 2004). In addition, threshold responses of environmental systems (e.g., lake overflows) may have been responsible for the abruptness of changes in some climatic records. This drought event has been proposed to represent the actual end of the AHP (Marshall et al., 2011).

It is noted that both events were so severe that they had a large impact on population dynamics in northern Africa as illustrated by the changes in phases of human settlements reconstructed by Kuper and Kröpelin (2006). The drought event at 4.2 ka BP was also linked with the end of the Akkadian society in Mesopotamia and of the Old Kingdom in Egypt, which have both been dated at 4.17 ka BP (Cullen et al., 2000; Stanley et al., 2003).

### 6.2. Influence of changes in the Nile River regime on the bottom-water oxygenation

Millimeter-scale laminations prevail in core P362/2-33 for the period between 9.5 and 7.3 ka BP (Fig. 8). The lithology of this part of the core is similar to laminated sediments described in another sediment core from the Nile deep-sea fan, which were interpreted as hyperpycnal flows forming during seasonal Nile floods (see Section 3.1) (Ducassou et al., 2008). The preservation of these seasonal laminations implies that bioturbation was prevented due to very high sedimentation rates and low bottom-water oxygen levels (Rossignol-Strick et al., 1982; Ducassou et al., 2008). The $O_2$-depletion occurred throughout the Mediterranean Basin and has been related to the large influx of fresh water and nutrients from the Nile River, which essentially shut down the Mediterranean thermohaline circulation and enhanced primary productivity (Rossignol-Strick et al., 1982; De Lange et al., 2008).

At the location of core P362/2-33, a short period of re-oxygenation of the bottom waters occurred between 8.2 and 7.8 ka BP, as indicated by the non-laminated or faintly-laminated sediments that contain opportunistic benthic foraminifera (such as the genii *Uvigerina, Bolivina* and *Bullimina*), which are intolerant to $O_2$-depleted conditions (Jorissen, 1999). This period of re-oxygenation coincided with the pronounced decrease in Blue Nile discharge (and erosional activity) at 8.5–7.3 ka BP (Fig. 8f and g).

Permanent improvement of oxygenation conditions occurred at 7.3 ka BP, as indicated by the clear evidence of bioturbation in younger sediments younger than 7.3 ka BP. This transition coincided with a marked decrease in both river runoff and relative intensity of the Blue Nile discharge at 7.3 ka BP (Fig. 8b, c and f). Therefore, our record clearly demonstrates that changes in Nile runoff accompanied by important switches in the fluvial source areas exerted a major control on bottom-water oxygenation on the Nile deep-sea fan.

## 7. Conclusions

We present a continuous and high-resolution record of changes in the Nile River regime that covers the past 9.5 kyr. By combining bulk elemental content, grain-size distribution and Nd and Sr radiogenic isotopes in a marine sediment core recovered on the Nile deep-sea fan, we were able to reconstruct changes in river runoff as well as changes in contribution from the two main sources, the Blue Nile and White Nile. The gradual decrease in river runoff between 8 and 4 ka BP was likely related to the decline in monsoonal precipitation, which followed the decrease in summer insolation at low latitudes. The changes in the source of fluvial sediments show a different picture with the Blue Nile being the main contributor during the early Holocene (10–8.5 ka BP) and the White Nile being a significant contributor between 8 and 4 ka BP. We propose that these changes were mainly forced by changes in autumn/spring insolation at low latitudes. Enhanced relative contribution from the Blue Nile occurred during the early and late Holocene, but was associated to high erosional activity only during the early Holocene, at times of high river runoff. This is best explained by the changes in orbital configuration during the Holocene, with the seasonality being in phase with that of today during the early Holocene but with insolation levels increased by ∼ 10% compared to today. The increase in relative contribution from the White Nile between 8 and 4 ka BP might be related to the shift of the peak of insolation toward the autumn, with insolation levels being ∼ 6% higher than today.

Our reconstruction of changes in river regime also documented a more abrupt centennial climatic fluctuation at 8.5–7.3 ka BP and a peak in aridity at 4.3–3.7 ka BP. The event at 8.5–7.3 ka BP has already been identified in other records from northeastern Africa and was generally associated to drier conditions. In our record, it is characterized by an abrupt decrease in contributions from the Blue Nile and in erosional activity and by an improvement of bottom-water oxygenation, which confirms the major influence of changes in Nile regime on the marine environment. Although our record does not allow to state whether this abrupt changes did lead or lag the 8.2 ka BP cooling event in the North Atlantic, it clearly highlights the existence of climatic teleconnections between high- and low-latitudes. The drought event at 4.3–3.7 ka is characterized by an increase in dust input and by a slight decrease in relative intensity of the Blue Nile discharge and represents the culmination of the long-term gradual drying of the Nile watershed. This drought event was already proposed to represent the actual end of the African Humid Period.

# References

Adamson, D.A., Gasse, F., Street, F.A., Williams, M.A.J., 1980. Late Quaternary history of the Nile. Nature 288, 50–55.

Alley, R.B., Mayewski, P.A., Sowers, T., Stuiver, M., Taylor, K.C., Clark, P.U., 1997. Holocene climatic instability: a prominent, widespread event 8200 yr ago. Geology 25, 483–486.

Billi, P., el Badri Ali, O., 2010. Sediment transport of the Blue Nile at Khartoum. Quat. Int. 226, 12–22.

Blaauw, M., Christen, J., 2011. Flexible paleoclimate age-depth models using an autoregressive gamma process. Bayesian Anal. 6, 457–474.

Box, M., Krom, M., Cliff, R., Bar-Matthews, M., Almogi-Labin, A., Ayalon, A., Paterne, M., 2011. Response of the Nile and its catchment to millennial-scale climatic change since the LGM from Sr isotopes and major elements of East Mediterranean sediments. Quat. Sci. Rev. 30, 431–442.

Brovkin, V., Bendsten, J., Claussen, M., Ganopolski, A., Kubatzki, C., Petoukhov, V., Andreev, A., 2002. Carbon cycle, vegetation, and climate dynamics in the Holocene: experiments with the CLIMBER-2 model. Global Biogeochem. Cycles 16.

Claussen, M., Kubatzki, C., Brovkin, V., Ganopolski, A., Hoelzmann, P., Pachur, H.J., 1999. Simulation of an abrupt change in Saharan vegetation in the mid-Holocene. Geophys. Res. Lett. 26, 2037–2040.

Cohen, R.K., O'Nions, A.S., Siegenthaler, R., Griffin, W.L., 1988. Chronology of the pressure–temperature history recorded by a granulite terrain. Contrib. Mineral. Petrol. 98, 303–311.

Collins, J.A., Schefuß, E., Heslop, D., Mulitza, S., Prange, M., Zabel, M., Tjallingii, R., Dokken, T.M., Huang, E., Mackensen, A., Schulz, M., Tian, J., Zarriess, M., Wefer, G., 2011. Interhemispheric symmetry of the tropical African rainbelt over the past 23,000 years. Nat. Geosci. 4, 42–45.

Cullen, H.M., deMenocal, P.B., Hemming, S., Hemming, G., Brown, F.H., Guilderson, T., Sirocko, F., 2000. Climate change and the collapse of the Akkadian empire: evidence from the deep sea. Geology 28, 379–382.

De Lange, G.L., Thompson, J., Reitz, A., Slomp, C.P., Principato, M.S., Erba, E., Corselli, C., 2008. Synchronous basin-wide formation and redox-controlled preservation of a Mediterranean sapropel. Nat. Geosci. 1, 606–610.

deMenocal, P., Ortiz, J., Guilderson, T., Adkins, J., Sarnthein, M., Baker, L., Yarusinsky, M., 2000a. Abrupt onset and termination of the African Humid period: rapid climate responses to gradual insolation forcing. Quat. Sci. Rev. 19, 347–361.

deMenocal, P., Ortiz, J., Guilderson, T., Sarnthein, M., 2000b. Coherent high- and low-latitude climate variability during the Holocene warm period. Science 288, 2198–2202.

Drake, N., Blench, R., Armitage, S., Bristow, C., White, K., 2011. Ancient watercourses and biogeography of the Sahara explain the peopling of the desert. Proc. Natl. Acad. Sci. USA. 108, 458–462.

Ducassou, E., Mulder, T., Migeon, S., Gonthier, E., Murat, A., Revel, M., Capotondi, L., Bernasconi, S.M., Mascle, J., Zaragosi, S., 2008. Nile floods recorded in deep Mediterranean sediments. Quat. Res. 70, 382–391.

Everitt, B.S., Hothorn, T., 2006. A Handbook of Statistical Analyses using R. Chapman & Hall/CRC, Boca Raton, FL, USA.

Facorellis, Y., Maniatis, Y., 1998. Apparent $^{14}$C ages of marine mollusk shells from a Greek island: calculation of the marine reservoir effect in the Aegean Sea. Radiocarbon 40, 963–973.

Feseker, T., Brown, K., Blanchet, C., Scholz, F., Nuzzo, M., Reitz, A., Schmidt, M., Hensen, C., 2010. Active mud volcanoes on the upper slope of the western Nile deep-sea fan—first results from the P362/2 cruise of R/V Poseidon. Geo-Mar. Lett. 30, 169–186, http://dx.doi.org/10.1007/s00367-010-0192-0.

Fleitmann, D., Burns, S.J., Mudelsee, M., Neff, U., Kramers, J., Mangini, A., Matter, A., 2003. Holocene forcing of the Indian Monsoon recorded in a stalagmite from southern Oman. Science 300, 1737–1739.

Froelich, P., Klinkhammer, G., Bender, M., Luedtke, N., Heath, G., Cullen, D., Dauphin, P., Hammond, D., Hartman, B., Maynard, V., 1979. Early oxidation of organic matter in pelagic sediments of the eastern equatorial Atlantic: suboxic diagenesis. Geochim. Cosmochim. Acta 43, 1075–1090.

Garcin, Y., Junginger, A., Melnick, D., Olago, D.O., Strecker, M.R., Trauth, M.H., 2009. Late Pleistocene–Holocene rise and collapse of Lake Suguta, northern Kenya Rift. Quat. Sci. Rev. 28, 911–925.

Garcin, Y., Melnick, D., Strecker, M.R., Olago, D., Tiercelin, J.J., 2012. East African mid-Holocene wet-dry transition recorded in palaeo-shorelines of Lake Turkana, northern Kenya Rift. Earth Planet. Sci. Lett. 331–332, 322–334.

Gasse, F., 2000. Hydrological changes in the African tropics since the last glacial maximum. Quat. Sci. Rev. 19, 189–211.

Gasse, F., Van Campo, E., 1994. Abrupt post-glacial climate events in West Asia and North Africa monsoon domains. Earth Planet. Sci. Lett. 126, 435–456.

Goiran, J.P., 2001. Recherche Géomorphologique dans la région littorale d'Alexandrie, Egypte: mobilité des paysages à l'Holocène récent et évolution des milieux portuaires antiques. Ph.D. Thesis. Université de Provence, Marseille, France.

Grootes, P., Stuiver, M., White, J.W.C., Johnsen, S., Jouzel, J., 1993. Comparison of oxygen isotope records from the GISP2 and GRIP Greenland ice cores. Nature 366, 552–554.

Guerzoni, S., Molinari, E., Chester, R., 1997. Saharan dust inputs to the western Mediterranean Sea: depositional patterns, geochemistry and sedimentological implications. Deep-Sea Res. 44, 631–654.

Gutjahr, M., Frank, M., Stirling, C.H., Klemm, V., van de Flierdt, T., Halliday, A.N., 2007. Reliable extraction of a deepwater trace metal isotope signal from Fe–Mn oxyhydroxide coatings of marine sediments. Chem. Geol. 242, 351–370.

Haug, G., Hughen, K., Sigman, D., Peterson, L., Röhl, U., 2001. Southward migration of the intertropical convergence zone through the Holocene. Science 293, 1304–1307.

Herut, B., Nimmo, M., Medway, A., Chester, R., Krom, M.D., 2001. Dry atmospheric inputs of trace metals at the Mediterranean coast of Israel (SE Mediterranean): sources and fluxes. Atmos. Environ. 35, 803–813.

Hijma, M.P., Cohen, K.M., 2010. Timing and magnitude of the sea-level jump preluding the 8200 yr event. Geology 38, 275–278.

Hillaire-Marcel, C., de Vernal, A., Piper, D.J.W., 2007. Lake Agassiz final drainage event in the northwest North Atlantic. Geophys. Res. Lett. 34.

Horwitz, E., Chiarizia, R., Dietz, M., 1992. A novel strontium-selective extraction chromatographic resin. Solvent Extr. Ion Exch. 10, 313–336.

Hughen, C.A., Lehman, S., Southon, J., Overpeck, J., Marchal, O., Herring, C., Turnbull, J., 2004. $^{14}$C activity and global carbon cycle changes over the past 50,000 years. Science 303, 202–207.

Jacobsen, S.B., Wasserburg, G.J., 1980. Sm–Nd isotopic evolution of chondrites. Earth Planet. Sci. Lett. 50, 139–155.

Jørgensen, B.B., Kasten, S., 2006. Sulfur cycling and methane oxidation. In: Schulz, H.D., Zabel, M. (Eds.), Marine Geochemistry. Springer-Verlag, Berlin, Heidelberg, New York, pp. 271–310.

Jorissen, F., 1999. Benthic foraminiferal successions across Late Quaternary Mediterranean sapropels. Mar. Geol. 153, 91–101.

Jung, S.J.A., Davies, G.R., Ganssen, G.M., Kroon, D., 2004. Stepwise Holocene aridification in NE Africa deduced from dust-borne radiogenic isotope records. Earth Planet. Sci. Lett. 221, 27–37.

Kim, J.H., Meggers, H., Rimbu, N., Lohmann, G., Freudenthal, T., Müller, P.J., Schneider, R.R., 2007. Impacts of the North Atlantic gyre circulation on Holocene climate off northwest Africa. Geology 35, 387–390.

Krom, M.D., Michard, A., Cliff, R.A., Strohle, K., 1999. Sources of sediment to the Ionian Sea and Western Levantine basin of the Eastern Mediterranean during S-1 sapropel times. Mar. Geol. 160, 45–61.

Krom, M.D., Stanley, J.D., Cliff, R.A., Woodward, J.C., 2002. Nile River sediment fluctuation over the past 7000 yr and their role in sapropel development. Geology 30, 71–74.

Kröpelin, S., Verschuren, L., Eggermont, H., Coquyt, C., Francus, P., Cazet, J.P., Fagot, M., Rumes, B., Russel, J.M., Darius, F., Conley, D.J., Schuster, M., von Suchodoletz, H., Engstrom, D.R., 2008. Climate-driven ecosystem succession in the Sahara: the past 6000 years. Science 320, 765–768.

Krumm, S., 2006. SediCalc. GeoZentrum Nordbayern. Erlangen, Germany.

Kucera, M., Malmgren, B.A., 1998. Logratio transformation of compositional data: a resolution of the constant sum constraint. Mar. Micropaleontol. 34, 117–120.

Kuper, R., Kröpelin, S., 2006. Climate-controlled Holocene occupation in the Sahara: motor of Africa's evolution. Science 313, 803–807.

Laskar, J., Robutel, P., Joutel, F., Gastineau, M., Correia, A.C.M., Levrard, B., 2004. A long term numerical solution for the insolation quantities of the Earth. Astron. Astrophys. 428, 261–285.

Lézine, A.M., Hély, C., Grenier, C., Braconnot, P., Krinner, G., 2011. Sahara and Sahel vulnerability to climate changes, lessons from Holocene hydrological data. Quat. Sci. Rev. 30, 3001–3012.

Liu, Z., Wang, Y., Gallimore, R., Gasse, F., Johnson, T., deMenocal, P., Adkins, J., Notaro, M., Prentice, I.C., Kutzbach, J., Jacob, R., Behling, P., Wang, L., Ong, E., 2007. Simulating the transient evolution and abrupt change of Northern Africa atmosphere–ocean–terrestrial ecosystem in the Holocene. Quat. Sci. Rev. 26, 1818–1837.

Marriner, N., Flaux, C., Kaniewski, D., Morhange, C., Leduc, G., Moron, V., Chen, Z., Gasse, F., Empereur, J.Y., Stanley, J.D., 2012. ITCZ and ENSO-like pacing of Nile delta hydro-geomorphology during the Holocene. Quat. Sci. Rev. 45, 73–84.

Marshall, M.H., Lamb, H.F., Huws, D., Davies, S.J., Bates, R., Bloemendal, J., Boyle, J., Leng, M.J., Umer, M., Bryant, C., 2011. Late Pleistocene and Holocene drought events at Lake Tana, the source of the Blue Nile. Global Planet. Change 78, 147–161.

Marzin, C., Braconnot, P., 2009. Variations of Indian and African monsoons induced by insolation changes at 6 and 9.5 kyr BP. Climate Dyn. 33, 215–231.

Mercone, D., Thomson, J., Croudace, I.W., Siani, G., Paterne, M., Troelstra, S., 2000. Duration of S1, the most recent sapropel in the eastern Mediterranean Sea, as indicated by accelerator mass spectrometry radiocarbon and geochemical evidence. Paleoceanography 15, 336–347.

Moulin, C., Lambert, C.E., Dulac, F., Dayan, U., 1997. Control of atmospheric export of dust from North Africa by the North Atlantic Oscillation. Nature 387, 691–693.

Nicholson, S.E., 2000. The nature of rainfall variability over Africa on time scales of decades to millennia. Global Planet. Change 26, 137–158.

Pachur, H.J., Kröpelin, S., 1987. Wadi Howar: paleoclimatic evidence from an extinct river system in the southeastern Sahara. Science 237, 298–300.

Padoan, M., Garzanti, E., Harlavan, Y., Villa, I.M., 2011. Tracing Nile sediment sources by Sr and Nd isotope signatures (Uganda, Ethiopia, Sudan). Geochim. Cosmochim. Acta 75, 3627–3644.

Prospero, J.M., Ginoux, P., Torres, O., Nicholson, S.E., Gill, T.E., 2002. Environmental characterization of global sources of atmospheric soil dust identified with the NIMBUS 7 total ozone mapping spectrometer (TOMS) absorbing aerosol product. Rev. Geophys. 40.

R Development Core Team, 2011. R: A Language and Environment for Statistical Computing. R Foundation for Statistical Computing. Vienna, Austria. ISBN 3-900051-07-0.

Reimer, P.J., Baillie, M.G.L., Bard, E., Bayliss, A., Beck, J.W., Blackwell, P.G., Bronk-Ramsey, C., Buck, C.E., Burr, G.S., Edwards, R.L., Friedrich, M., Grootes, P.M., Guilderson, T.P., Hajdas, I., Heaton, T.J., Hogg, A.G., Hughen, K.A., Kaiser, K.F., Kromer, B., McCormac, F.G., Manning, S.W., Reimer, R.W., Richards, D.A., Southon, J.R., Talamo, S., Turney, C.S.M., van der Plicht, J., Weyhenmeyer, C.E., 2009. INTCAL09 and MARINE09 radiocarbon age calibration curves 0–50,000 years cal BP. Radiocarbon 51, 1111–1150.

Reitz, A., Thomson, J., de Lange, G.J., Hensen, C., 2006. Source and development of large manganese enrichments above eastern Mediterranean sapropel S1. Paleoceanography 21.

Renssen, H., Brovkin, V., Fichefet, T., Goose, H., 2003. Holocene climate instability during the termination of the African Humid Period. Geophys. Res. Lett. 30.

Renssen, H., Goosse, H., Fichefet, T., 2007. Simulation of Holocene cooling events in a coupled climate model. Quat. Sci. Rev. 26, 2019–2029.

Revel, M., Ducassou, E., Grousset, F., Bernasconi, S., Migeon, S., Revillon, S., Mascle, J., Murat, A., Zaragosi, S., Bosch, D., 2010. 100,000 years of African monsoon variability recorded in sediments of the Nile margin. Quat. Sci. Rev. 29, 1342–1362.

Rossignol-Strick, M., 1983. African monsoons, an immediate climate response to orbital insolation. Nature 304, 46–49.

Rossignol-Strick, M., Nesteroff, W., Olive, P., Vergnaud-Grazzini, C., 1982. After the deluge: Mediterranean stagnation and sapropel formation. Nature 295, 105–110.

Ruddiman, W.F., 2003. The anthropogenic greenhouse era began thousands of years ago. Climatic Change 61, 261–293.

Shanahan, T.M., Overpeck, J.T., Sharp, W.E., Scholz, C.A., Arko, J.A., 2007. Simulating the response of a closed-basin lake to recent climate changes in tropical West Africa (Lake Bosumtwi, Ghana). Hydrol. Processes 21, 1678–1691.

Siani, G., Paterne, M., Michel, E., Sulpizio, R., Sbrana, A., Arnold, M., Haddad, G., 2001. Mediterranean sea surface radiocarbon reservoir age changes since the Last Glacial Maximum. Science 294, 1917–1920.

Stager, J.C., Cumming, B.F., Meeker, L.D., 2003. A 10,000-year high-resolution diatom record from Pilkington Bay, Lake Victoria, East Africa. Quat. Res. 59, 172–181.

Stanley, J.D., Krom, M.D., Cliff, R.A., Woodward, J.C., 2003. Short contribution: Nile flow failure at the end of the Old Kingdom, Egypt: strontium isotopic and petrologic evidence. Geoarchaeology 18, 395–402.

Stuiver, M., Reimer, P.J., Reimer, R., 2005. Calib 5.0.

Thompson, L.G., Mosley-Thompson, E., Davis, M.E., Henderson, K.A., Brecher, H.H., Zagorodnov, V.S., Mashiotta, T.A., Lin, P.N., Mikhalenko, V.N., Hardy, D.R., Beer, J., 2002. Kilimanjaro ice core records: evidence of Holocene climate change in tropical Africa. Science 298, 589–593.

Tjallingii, R., Claussen, M., Stuut, J.B.W., Fohlmeister, J., Jahn, A., Bickert, T., Lamy, F., Röhl, U., 2008. Coherent high- and low-latitude control of the northwest African hydrological balance. Nat. Geosci. 1, 670–675.

Tjallingii, R., Röhl, U., Kölling, M., Bickert, T., 2007. Influence of the water content on X-ray fluorescence core-scanning measurements in soft marine sediments. Geochem. Geophys. Geosyst. 8.

Verardo, D.J., Froelich, P.N., McIntyre, A., 1990. Determination of organic carbon and nitrogen in marine sediments using the Carlo Erba NA-1500 Analyser. Deep-Sea Res. 37, 157–165.

Verschuren, D., Sinninghe Damste, J.S., Moernaut, J., Kristen, I., Blaauw, M., Fagot, M., Haug, G.H., 2009. Half-precessional dynamics of monsoon rainfall near the East African Equator. Nature 462, 637–641.

Wang, S., Zhou, T., Cai, J., Zhu, J., Xie, Z., Gong, D., 2004. Abrupt climate change around 4 ka BP: role of the thermohaline circulation as indicated by a GCM experiment. Adv. Atmos. Sci. 21, 291–295, http://dx.doi.org/10.1007/BF02915716.

Wang, Y.J., Cheng, H., Edwards, R.L., An, Z.S., Wu, J.Y., Shen, C.C., Dorale, J.A., 2001. A high-resolution absolute-dated late Pleistocene monsoon record from Hulu Cave, China. Science 294, 2345–2348.

Weltje, G.J., 1997. End-member modeling of compositional data: numerical–statistical algorithms for solving the explicit mixing problem. Math. Geol. 29, 503–549.

Weltje, G.J., Prins, M.A., 2003. Muddled or mixed? Inferring palaeoclimate from size distributions of deep-sea clastics. Sediment. Geol. 162, 39–62.

Weltje, G.J., Tjallingii, R., 2008. Calibration of XRF core scanners for quantitative geochemical logging of sediment cores: theory and application. Earth Planet. Sci. Lett. 274, 423–438.

Williams, M.A., 2009. Late Pleistocene and Holocene environments in the Nile basin. Global Planet. Change 69, 1–15.

Williams, M.A.J., Adamson, D.A., 1974. Late Pleistocene desiccation along the White Nile. Nature 248, 584–585.

Williams, M.A.J., Talbot, M., Aharon, P., AbdlSalaam, Y., Williams, F., Brendeland, K.I., 2006. Abrupt return of the summer monsoon 15,000 years ago: new supporting evidence from the lower White Nile valley and Lake Albert. Quat. Sci. Rev. 15, 2651–2665.